Simulation of laminar impinging jet on a porous medium with a thermal non-equilibrium model

Felipe T. Dórea, Marcelo J.S. de Lemos *

Departamento de Energia – IEME, Instituto Tecnológico de Aeronáutica – ITA, 12228-900 - São José dos Campos - SP, Brazil

ARTICLE INFO

ABSTRACT

This work shows numerical simulations of an impinging jet on a flat plate covered with a layer of a porous material. Macroscopic equations for mass and momentum are obtained based on the volume-average concept. Two macroscopic models are employed for analyzing energy transport, namely the one-energy equation model, based on the Local Thermal Equilibrium assumption (LTE), and the two-energy equation closure, where distinct transport equations for the fluid and the porous matrix follow the Local Non-Thermal Equilibrium hypothesis (LNTE). The numerical technique employed for discretizing the governing equations was the finite volume method with a boundary-fitted non-orthogonal coordinate system. The SIMPLE algorithm was used to handle the pressure–velocity coupling. Parameters such as porosity, porous layer thickness, material permeability and thermal conductivity ratio were varied in order to analyze their effects on flow and heat transport. Results indicate that for low porosities, low permeabilities, thin porous layers and for high thermal conductivity ratios, a different distribution of local Nusselt number at the wall is calculated depending on the energy model applied. The use of the LNTE model indicates that it is advantageous to use a layer of highly conducting and highly porous material attached to the hot wall.

1. Introduction

Modern industrial equipment makes use of impinging jets in order to locally cool, heat or dry surfaces. These applications include electronics cooling, glass tempering, annealing of metals, drying of textiles products and anti-ice systems for aircraft safety, for example. The main advantage of impinging jets is their ability to produce high localized mass and heat transfer rates due to the thin boundary layer around the flow stagnation region.

Pioneering studies considering two-dimensional impinging jets with low Reynolds number, onto uncovered flat walls, are presented in Gardon and Akfirat [1], who experimentally obtained local and averaged heat transfer coefficients. Sparrow and Wong [2] made use of the well-known heat and mass transfer analogy and took experimental data on local mass transfer for a two-dimensional impinging jet. Results were then converted to heat transfer using the mentioned technique. Chen et al. [3] experimentally and numerically analyzed mass and heat transfer induced by a two-dimensional laminar jet. Chiriac and Ortega [4] performed numerical simulations in steady and transitory regime for a two-dimensional jet impinging against a plate with constant temperature. In addition, in the recent years a number of research papers covered a wide range of studies in porous media [5–18], including

flows parallel to a layer of porous material [19] across permeable baffles [20,21] and porous inserts [22]. Investigation on configurations concerning perpendicular jets into a porous core is much needed for optimization of heat sinks attached to solid surfaces. However, studies of porous medium under impinging jets are, unfortunately, yet very scarce in the literature. An example found are those given by numerical simulations of Kim and Kuznetsov [23], who investigated optimal characteristics of impinging jets into heat sinks. Another innovative application of impinging jets, such as fiber hydroentalglement, can also be found in the recent literature [24,25].

As mentioned, for the specific case here investigated, i.e., an impinging jet over a covered plate, there are not too many results in the open literature, being one example the work of Prakash et al. [26,27] who obtained a flow visualization of turbulent jets impinging against a porous medium. Also, Fu and Huang [28] evaluated the thermal performance of different porous layers under a impinging jet and Jeng and Tzeng [29] studied the hydrodynamic and thermal performance of a jet impinging on a metallic foam. Graminho and de Lemos [30] investigated the flow structure of a laminar jet impinging on a layer of porous material. In [30] a laminar version of a mathematical model described in detail by de Lemos [31], who worked on a macroscopic two-equation model for turbulent flow in porous media, was applied. Previously, Rocamora and de Lemos [32] had added thermal modeling for the treatment of a permeable medium. Later, de Lemos and Fischer

* Corresponding author.
   E-mail address: delemos@ita.br (M.J.S. de Lemos).

Nomenclature

A_i	Macroscopic interface area between the porous region and the clear flow	Re	Reynolds number based on the channel height, $Re = \rho v_0 B/\mu$
B	Jet width	S_φ	Source term
c_F	Forchheimer coefficient.	T	Temperature
Da	Darcy number, $Da = K/H^2$	$\langle \mathbf{u} \rangle^i$	Intrinsic (fluid) average of $\mathbf{u}$
H	Channel height	$\mathbf{u}_D$	Darcy velocity vector (volume-average over $\mathbf{u}$) $= \phi \langle \mathbf{u} \rangle^i$
h	Porous layer thickness, film coefficient	x, y	Cartesian coordinates
K	Permeability		
k_{eff}	Effective thermal conductivity	*Greek symbols*	
k	Thermal conductivity	μ	Dynamic viscosity
L	Channel length	ρ	Density
Nu	Nusselt number		
Nu_f	Fluid phase Nusselt number	*Symbols, subscripts, special characters*	
Nu_s	Solid Phase Nusselt number	s,f	solid, fluid
p	Thermodynamic pressure	w	wall
q_w	Integral wall heat flux	ϕ	Related to porous medium
q_w^ϕ	Integral wall heat flux will porous layer	o	Inlet conditions
$\langle p \rangle^i$	Intrinsic (fluid) average of pressure		

[33] added the Local Thermal Equilibrium energy model (LTE) to the flows analysis in [30].

The objective of the present contribution is to extend the work of [33] in order to consider now a two-energy equation model, which is based on the Local Thermal Non-Equilibrium assumption (LTNE). Both sets of results, from LTE and LTNE closures, are here compared in order to access their performance in evaluating under which circumstances the addition of a layer of thermally conducting porous material can enhance the overall heat transferred from a surface.

2. Confined impinging jet

The cases here investigated and their corresponding nomenclatures are detailed in Fig. 1. A laminar jet with uniform velocity v_o and constant temperature T_o enters through a gap into a channel with height H and length $2L$ (Fig. 1(a)). Fluid impinges normally against the bottom plate yielding a two-dimensional confined impinging jet configuration. The width of the inlet nozzle is B and the bottom plate temperature, T_1, is maintained constant and 10 K above the temperature of the incoming jet, T_o. In a different
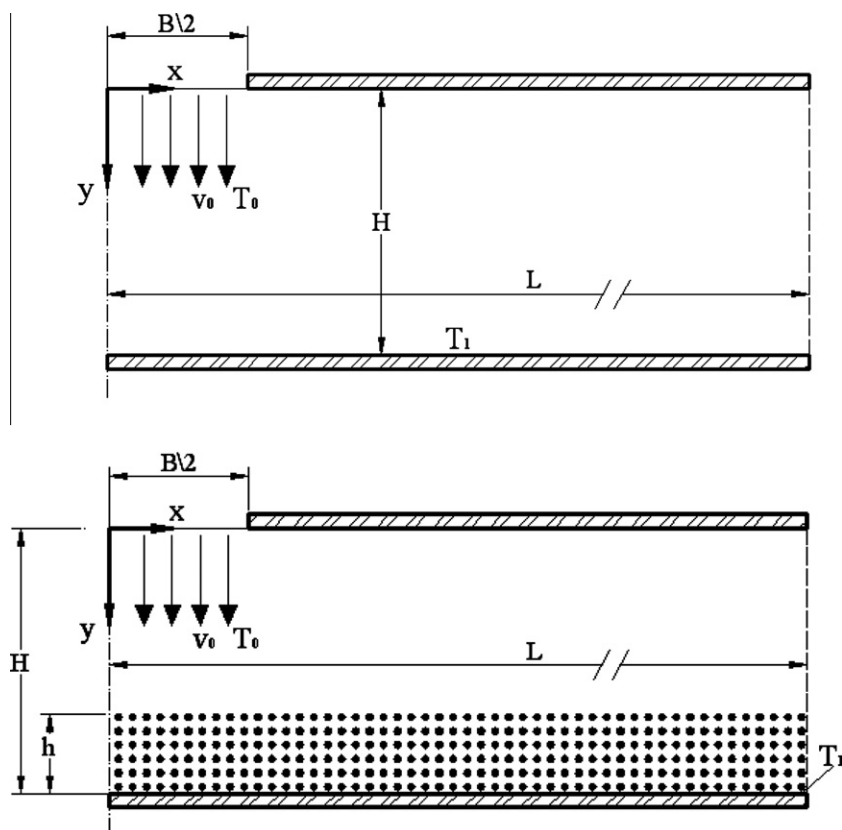

Fig. 1. Cases investigated: (a) Confined impinging jet on a flat plate – clear medium case (b) Confined impinging jet on a plate covered with a layer of porous material – porous case.

configuration, the bottom surface is covered with a porous layer of height h (Fig. 1(b)). In both cases, the flow is assumed to be two-dimensional, laminar, incompressible and steady. Also, the porous medium is taken to be homogeneous, rigid and inert. Fluid properties are constant and gravity effects are neglected.

The boundary conditions for the problem are: (a) constant velocity and temperature of the entering jet, (b) no slip condition on the walls, (c) symmetry condition at $x = 0$, (d) fully developed flow at channel exit ($x = L$). At the bottom plate ($y = H$), constant temperature condition is assumed whereas along the upper wall, for $B/2 < x \leqslant L$, null heat flux condition prevails.

3. Mathematical modeling and numerics

As mentioned, the mathematical model here employed is described in de Lemos and Fischer [33] including now the assumption of Local Thermal Non-Equilibrium (LTNE) or two-energy equation model for heat transfer calculations. As most of the theoretical development is readily available in the open literature, the governing equations will be just presented and details about their derivations can be obtained in the above-mentioned papers. Essentially, local instantaneous equations are volume-averaged using appropriate mathematical tools [34]. Here, only laminar flow is considered since the Reynolds number based on the incoming jet

velocity is less than 1000. Due to the expansion of the flow when entering the channel, velocities everywhere will always be lower than that of the incoming jet, and for such reason it is here assumed that the flow remains laminar in both the fluid layer and within the porous substrate. Accordingly, for laminar flow, the equations read:

3.1. Macroscopic continuity equation

The macroscopic equation of continuity for an incompressible fluid flowing through a porous medium is given by:

$$\nabla \cdot \mathbf{u}_D = 0 \tag{1}$$

where, $\mathbf{u}_D$ is the average surface velocity, also known as Darcy velocity. In Eq. (1) the Dupuit–Forchheimer relationship, $\mathbf{u}_D = \phi \langle \mathbf{u} \rangle^i$, has been used where ϕ is the porous medium porosity and $\langle \mathbf{u} \rangle^i$ identifies the intrinsic (fluid phase) average of the local velocity vector $\mathbf{u}$ [34].

3.2. Macroscopic momentum equation

The macroscopic momentum equation (Navier–Stokes) for an incompressible fluid with constant properties flowing through a porous medium can be written as:
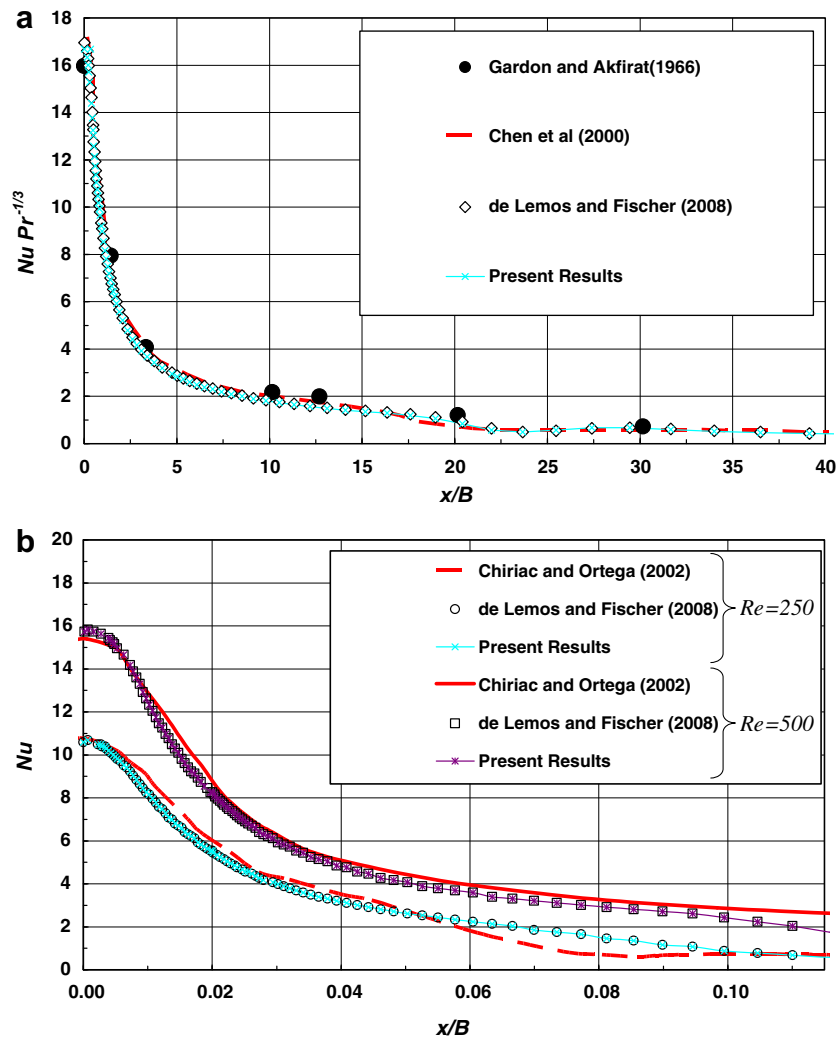

Fig. 2. Validation for distribution of Nu along the lower plate for clear channel: (a) $Re = 450$, $H/B = 4$; (b) $H/B = 5$.

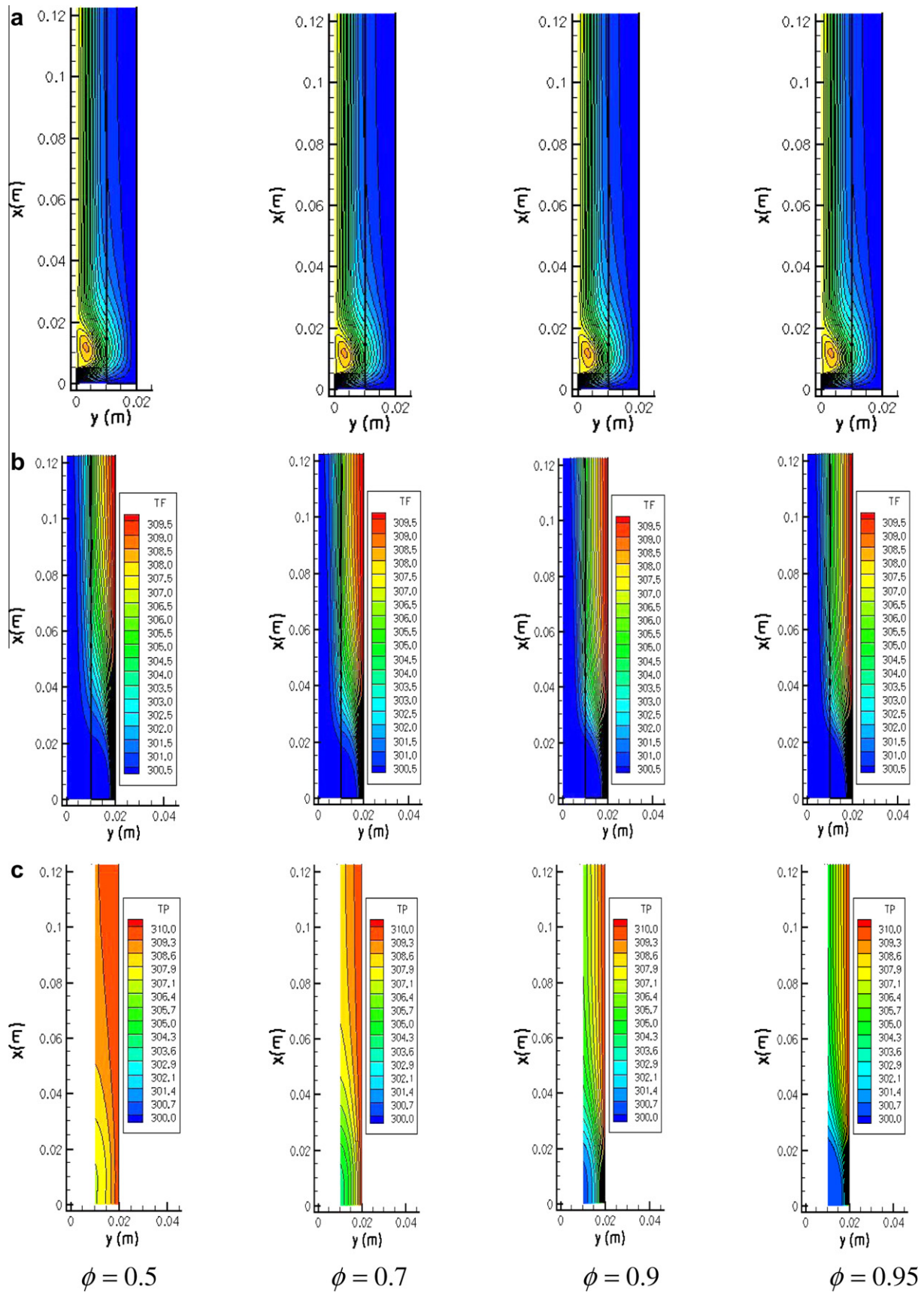**Fig. 3.** Effect of porosity for $Re = 750$, $H/B = 2$, $Da = 8.28x10^{-3}$, $h = 0.5H$, and $k_s/k_f = 10$: (a) streamlines, (b) fluid temperature, (c) solid temperature.

$$\rho \nabla \cdot \frac{\mathbf{u}_D \mathbf{u}_D}{\phi} = -\nabla \phi \langle p \rangle^i + \mu \nabla^2 \mathbf{u}_D - \left[\frac{\mu \phi}{K} \mathbf{u}_D + \frac{c_F \phi \rho}{\sqrt{K}} |\mathbf{u}_D| \mathbf{u}_D \right] \quad (2)$$

where the last two terms in Eq. (2) represent the Darcy and the Forchheimer terms, respectively. The symbol K is the porous medium permeability, $c_F = 0.55$ is the form drag coefficient, $\langle p \rangle^i$ is the intrinsic pressure of the fluid, ρ is the fluid density and μ represents the fluid viscosity.

3.3. One-energy equation model

The energy equation for laminar flow in porous medium, using the Local Thermal Equilibrium hypothesis (LTE), has been given in detail in the work of Rocamora and de Lemos [32], as follows:

$$(\rho c_p)_f \nabla \cdot \left(\mathbf{u}_D \langle T \rangle^i \right) = \nabla \cdot \left\{ \mathbf{K}_{eff} \cdot \nabla \langle T \rangle^i \right\} \quad (3)$$

where $\langle T \rangle^i$ and $\mathbf{K}_{eff}$ are the average temperature (fluid and solid) and the effective conductivity tensors, respectively. The effective conductive tensor, $\mathbf{K}_{eff}$, accounts for all mechanisms contributing to the energy budget, i.e., for laminar flow those mechanisms are effective conduction (fluid and solid), tortuosity and thermal dispersion due to spatial deviations of velocity and temperature. $\mathbf{K}_{eff}$ is then given by:

$$\mathbf{K}_{eff} = [\phi k_f + (1 - \phi)k_s]\mathbf{I} + \mathbf{K}_{tor} + \mathbf{K}_{disp} \quad (4)$$

where $\mathbf{I}$ is the unit tensor and $\mathbf{K}_{tor}$ and $\mathbf{K}_{disp}$ are defined such that [35],

$$\text{Tortuosity}: \left[\frac{1}{\Delta V} \int_{A_i} \mathbf{n}_i (k_f T_f - k_s T_s) dA \right] = \mathbf{K}_{tor} \cdot \nabla \langle T \rangle^i \quad (5)$$

$$\text{Thermal dispersion}: -(\rho c_p)_f \left(\phi \langle {}^i \mathbf{u}^i T_f \rangle^i \right) = \mathbf{K}_{disp} \cdot \nabla \langle T \rangle^i \quad (6)$$

In Eq. (5) $\mathbf{n}_i$ is the normal unit vector at the fluid–solid interface, pointing from the fluid towards the solid phase. A complete review of Eq. (3) is beyond the scope of the present text and details of its derivation can be found in references [32,35]. Here, it is sufficient to say that the mechanism of dispersion comes from decomposing in space the convection term, and then volume-averaging it [35]. Also, for the sake of simplicity, the mechanisms of tortuosity and dispersion are here neglected.

3.4. Two-energy equation model

The one-energy equation model seen above is usually valid when the temperature difference between the solid and fluid phase is relatively small. In this case, the condition of Local Thermal Equilibrium (LTE) is applied. When the LTE assumption is far from reality, the two-energy equation model treats the solid and the fluid energy balance on separate, via their own macroscopic energy equations [35]. Those equations read:

$$\underbrace{(\rho c_p)_f \left[\nabla \cdot \left\{ \phi \left(\langle \mathbf{u} \rangle^i \langle T_f \rangle^i + \langle {}^i \mathbf{u}^i T_f \rangle^i \right) \right\} \right]}_{\text{Convection}}$$

$$= \underbrace{\nabla \cdot \left[k_f \nabla \left(\phi \langle T_f \rangle^i \right) + \frac{1}{\Delta V} \int_{A_i} \mathbf{n}_i k_f T_f dA \right]}_{\text{conduction}} + \underbrace{\frac{1}{\Delta V} \int_{A_i} \mathbf{n}_i \cdot k_f \nabla T_f dA}_{\text{interfacial heat transfer}} \quad (7)$$

$$0 = \underbrace{\nabla \cdot \left\{ k_s \nabla \left[(1 - \phi) \langle T_s \rangle^i \right] - \frac{1}{\Delta V} \int_{A_i} \mathbf{n}_i k_s T_s dA \right\}}_{\text{conduction}}$$

$$\underbrace{- \frac{1}{\Delta V} \int_{A_i} \mathbf{n}_i \cdot k_s \nabla T_s dA}_{\text{interfacial heat transfer}} \quad (8)$$

where $\langle T_s \rangle^i$ and $\langle T_f \rangle^i$ denote the intrinsic average temperature of solid and fluid phases, respectively, and A_i is the interfacial area within the REV.

3.5. Interfacial heat transfer

In Eqs. (7) and (8) the heat transferred between the two phases can be modeled by means of a film coefficient h_i such that,

$$h_i a_i \left(\langle T_s \rangle^i - \langle T_f \rangle^i \right) = \frac{1}{\nabla V} \int_{A_i} \mathbf{n}_i \cdot k_f \nabla T_f dA = \frac{1}{\Delta V} \int_{A_i} \mathbf{n}_i \cdot k_s \nabla T_s dA \quad (9)$$

where $a_i = A_i / \nabla V$ is the interfacial area per unit volume. In porous media, the high values of a_i make them attractive for transferring thermal energy via conduction through the solid followed by convection to a fluid stream.

Wakao et al. [36] obtained a heuristic correlation for h_i for a closely packed bed of particle diameter D and compared their results with experimental data. This correlation for the interfacial heat transfer coefficient is given by,

$$\frac{h_i D}{k_f} = 2 + 1.1 Re_D^{0.6} Pr^{1/3} \quad (10)$$

Later, a numerical correlation for the interfacial convective heat transfer coefficient was proposed by Kuwahara et al. [37] for laminar flow as:

$$\frac{h_i D}{k_f} = \left(1 + \frac{4(1 - \phi)}{\phi} \right) + \frac{1}{2}(1 - \phi)^{1/2} Re_D Pr^{1/3},$$
$$\text{valid for } 0.2 < \phi < 0.9 \quad (11)$$

The interfacial heat transfer h_i introduced by Eq. (9) is calculated by Eq. (10) for $\phi > 0.9$ and Eq. (11) for $0.2 < \phi < 0.9$. The energy Eqs. (7) and (8) are then rewritten as:

$$(\rho c_p)_f \nabla \cdot \left(\mathbf{u}_D \langle T_f \rangle^i \right) = \nabla \cdot \left\{ \mathbf{K}_{eff,f} \cdot \nabla \langle T_f \rangle^i \right\} + h_i a_i \left(\langle T_s \rangle^i - \langle T_f \rangle^i \right) \quad (12)$$

$$0 = \nabla \cdot \left\{ \mathbf{K}_{eff,s} \cdot \nabla \langle T_s \rangle^i \right\} - h_i a_i \left(\langle T_s \rangle^i - \langle T_f \rangle^i \right) \quad (13)$$

where, $\mathbf{K}_{eff,f}$ and $\mathbf{K}_{eff,s}$ are the effective conductivity tensors for fluid and solid, respectively, given by:

$$\mathbf{K}_{eff,f} = [\phi k_f]\mathbf{I} + \mathbf{K}_{f,s} + \mathbf{K}_{disp} \quad (14)$$
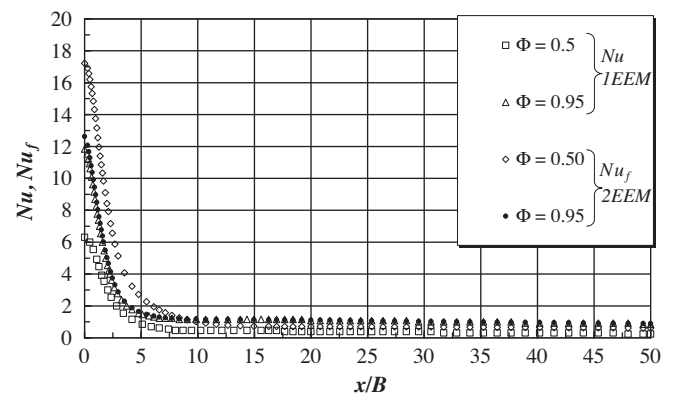$$\mathbf{K}_{eff,s} = [(1 - \phi)k_s]\mathbf{I} + \mathbf{K}_{s,f} \quad (15)$$

Fig. 4. Comparison of local Nusselt distribution as a function of energy model and porosity, $Re = 750$, $H/B = 2$, $k_s/k_f = 10$, $Da = 8.28 \times 10^{-3}$ and $h = 0.5H$: Nu, one-energy equation model (1EEM), Nu_f, two-energy equation model (2EEM).
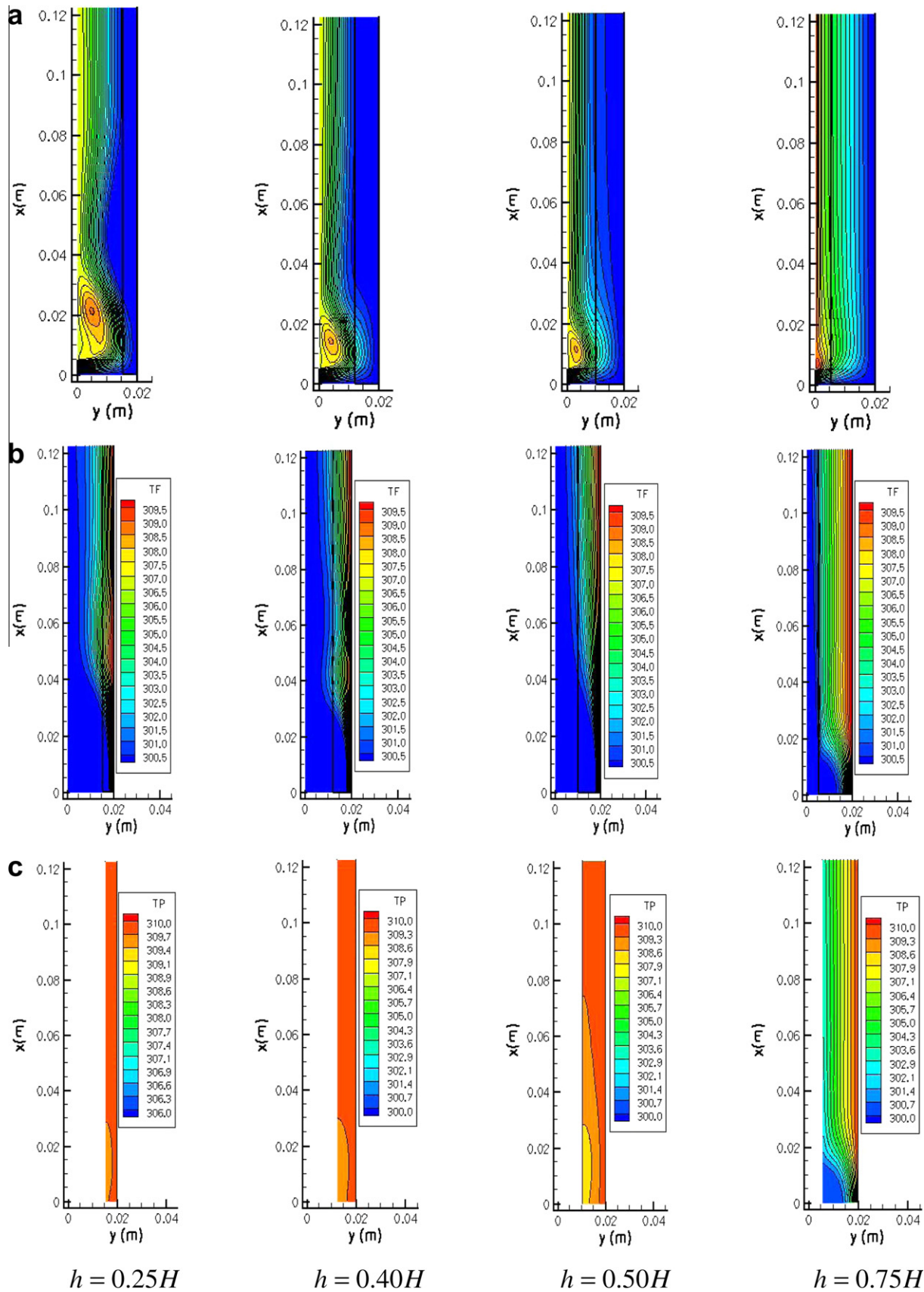
Fig. 5. Effect of porous layer thickness on temperature distributions for $Re = 750$, $H/B = 2$, $Da = 8.28 \times 10^{-3}$, $\phi = 0.9$, and $k_s/k_f = 10$: (a) streamlines, (b) fluid temperature, (c) solid temperature.

where $\mathbf{K}_{disp}$, $\mathbf{K}_{f,s}$ and $\mathbf{K}_{s,f}$ are coefficients defined as,

Thermal dispersion : $-(\rho c_p)_f(\phi\langle^i\mathbf{u}^i T_f\rangle^i) = \mathbf{K}_{disp} \cdot \nabla\langle T_f\rangle^i$ (16)

Local conduction :
$$\begin{cases} \nabla \cdot \left[\frac{1}{\Delta V}\int_{A_i}\mathbf{n}_i k_f T_f dA\right] = \mathbf{K}_{f,s}\cdot\nabla\langle T_s\rangle^i \\ -\nabla\cdot\left[\frac{1}{\Delta V}\int_{A_i}\mathbf{n}_i k_s T_s dA\right] = \mathbf{K}_{s,f}\cdot\nabla\langle T_f\rangle^i \end{cases}$$ (17)

In this work, for simplicity, one assumes that the overall thermal resistance between the two phases is controlled by the interfacial film coefficient rather than by the thermal resistance within each phase. As such, the local conduction coefficients $\mathbf{K}_{f,s}$, $\mathbf{K}_{s,f}$ are here neglected for the sake of simplicity. Also, for consistency with assumptions for the one-energy equation model, the mechanism of dispersion is here further neglected. Additional information on the models in Eqs. (14) and (15) can be found in [38].

3.6. Non-dimensional parameters

The local Nusselt number for the one-energy equation model used by de Lemos and Fischer [33] is given by:

$$Nu = \left(\frac{\partial\langle\overline{T}\rangle^i}{\partial y}\right)_{y=H}\frac{H}{T_1 - T_0}$$ (18)

Eq. (18) assumes the Local Thermal Equilibrium hypothesis, i.e., $\langle T\rangle^i = \langle T_s\rangle^i = \langle T_f\rangle^i$. When the Local Non-Thermal Equilibrium model is applied, that are distinct definitions for the Nusselt number associated to each phase, as follows [39]

Fluid phase Nusselt number:

$$Nu_f = \left(\frac{\partial\langle\overline{T_f}\rangle^i}{\partial y}\right)_{y=H}\frac{H}{T_1 - T_0}$$ (19)

Solid phase Nusselt number:

$$Nu_s = \left(\frac{\partial\langle\overline{T_s}\rangle^i}{\partial y}\right)_{y=H}\frac{H}{T_1 - T_0}$$ (20)

3.7. Numerical method

Eqs. (1), (2), (12) and (13) were discretized in a two-dimensional domain involving both the clear passage and the porous medium of Fig. 1(b) Cases simulating clear channels were obtained by setting $\phi = 1$, $K \rightarrow \infty$ and $c_F = 0$ everywhere in the computational domain.

The finite volume method was used in the discretization process and the SIMPLE algorithm [40] was applied to handle the pressure–velocity coupling. The discretized form of the two-dimensional conservation equation for a generic property φ in steady-state regime reads,

$$I_e + I_w + I_n + I_s = S_\varphi$$ (21)

where I_e, I_w, I_n and I_s represent, respectively, the fluxes of φ in the faces east, west, north and south faces of the control volume and S_φ is a term source.

Standard source term linearization is accomplished by using,

$$S_\varphi \approx S_\varphi^{**}\langle\varphi\rangle_p^i + S_\varphi^*$$ (22)

For the momentum equation, discretization in the x-direction gives,

$$S^{*x} = (S_e^{*x})_P - (S_w^{*x})_P + (S_n^{*x})_P - (S_s^{*x})_P + S_P^*$$ (23)
$$S^{**x} = S_\phi^{**}$$ (24)

where, S^{*x} is the diffusive part, here treated in an implicit form. The second term, S^{**x}, entails the additional drag forces due to the por-

ous matrix, last two terms in Eq. (2), which are here treated explicitly (see [30] for details).

For the numerical simulations here presented, a grid of 40×180 (7200) nodes was used, which was refined next to the jet entrance and close to the walls. Code validation and grid independency studies were conducted for the empty channel case and results were compared with the literature, as shown below. As mentioned, all results have been simulated with the following geometric configurations and boundary conditions: uniform inlet jet velocity, uniform inlet jet temperature, $T_o = 300$ K, bottom plate temperature, $T_1 = 310$ K; ratio between nozzle-to-plate distance and nozzle width, $H/B = 2$; nozzle width, $B = 1 \times 10^{-2}$ m and channel length, $L = 0.5$ m.

4. Results and discussion

4.1. Clear channel

The first set of results is related to the configuration shown in Fig. 1(a), where no porous material is attached to the bottom wall. Fig. 2(a) shows the distribution of the local Nusselt number close to the stagnation region compared with experimental data of Gardon and Akfirat [1], numerical results of Chen et al. [3] and predictions by de Lemos and Fischer [33]. In Fig. 2(a) the Reynolds number is
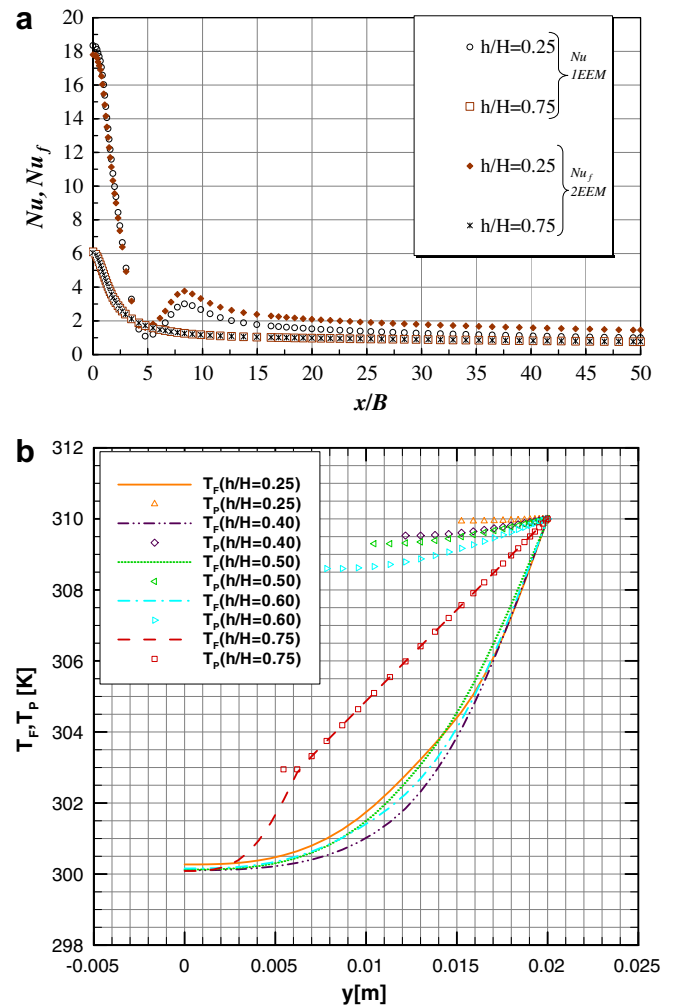
Fig. 6. Comparison of axial Nusselt distribution (a) and transversal temperature profiles at $x/B = 8$ (b) for several h/H. $Re = 750$, $H/B = 2$, $k_s/k_f = 10$, $Da = 8.28 \times 10^{-3}$, $\phi = 0.9$.

Re = 450, the inlet velocity profile at the jet inlet is fully developed and the fluid flows in between parallel plates. The temperature profile is uniform at the bottom wall and the ratio between the nozzle-to-plate spacing and nozzle width is H/B = 4. In order to make the comparison, it is necessary to normalize the local Nusselt with $Pr^{-1/3}$. The figure seems to indicate a good agreement with
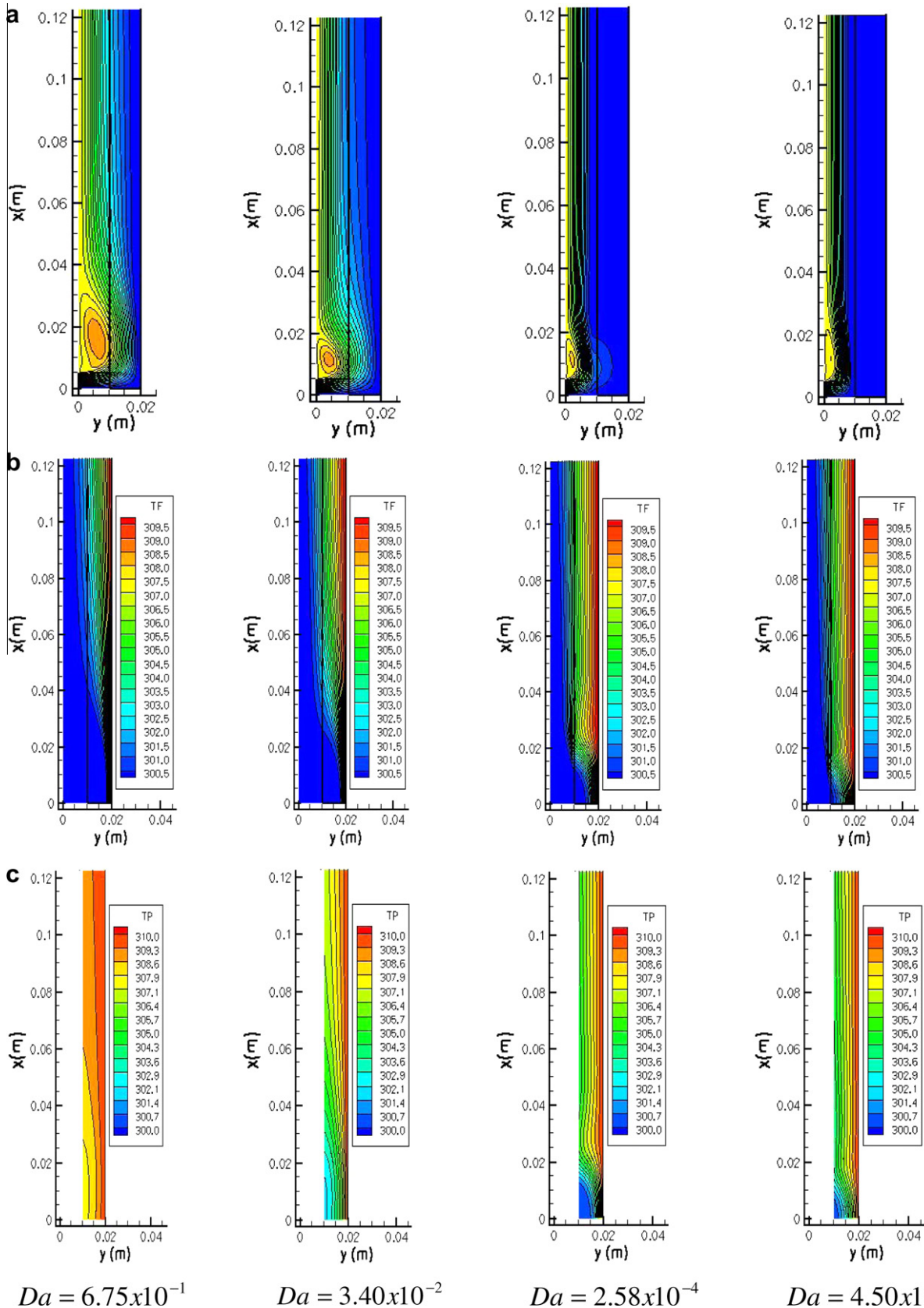

$$Da = 6.75x10^{-1} \qquad Da = 3.40x10^{-2} \qquad Da = 2.58x10^{-4} \qquad Da = 4.50x10^{-5}$$

Fig. 7. Effect of Da on flow and temperature distributions for Re = 750, H/B = 2, h = 0.5H, ϕ = 0.9, and k_s/k_f = 10: (a) streamlines, (b) fluid temperature, (c) solid temperature.
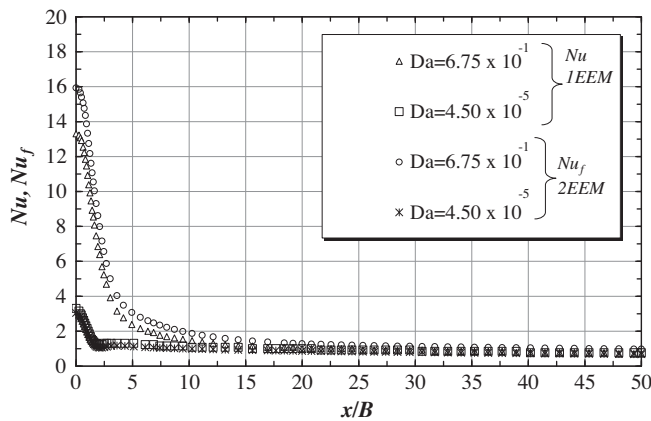
Fig. 8. Local Nusselt distribution as a function of Darcy number and energy model, $Re = 750$, $H/B = 2$, $k_s/k_f = 10$, $h = 0.5H$ and $\phi = 0.9$.

both numerical simulations and experimental measurements found in the literature. Fig. 2(b) shows a comparison of local Nusselt number at the lower plate with the numerical results of Chiriac and Ortega [4] and de Lemos and Fischer [33]. Inlet velocity and temperature profiles are uniform at the entrance slot and $H/B = 5$. One can see that here also a reasonable agreement with the literature is obtained for Reynolds number up to 500. In the end, Fig. 2 indicates the correctness of the code and suitability of the computational grid used.

4.2. Channel with porous layer

For cases with a permeable layer located at the bottom of the channel, the resulting configuration is shown in Fig. 1(b). The porous material is assumed to be rigid, with porosity ϕ, thermal conductivity ratio k_s/k_f, permeability K and non-dimensional thickness, h/H. Results below are obtained using distinct values for such four parameters. In this work, the permeability is considered to be a scalar that varies with the porosity and the particle diameter D_p, according to the Ergun equation (see [35]):

$$K = \frac{D_p^2 \phi^3}{144(1 - \phi^2)} \tag{25}$$

The Darcy number, Da, is defined by the ratio $Da = K/H^2$.

4.3. Effect of porosity, ϕ

Fig. 3 shows the streamlines and temperature fields for both the fluid and porous layer in the geometry of Fig. 1(b), as a function of the porosity ϕ. For clarity, the two-dimensional maps are turned 90 degrees to the left (counterclockwise), with the incoming jet located at the lower left corner of the drawings. Therefore, the fluid layer is located on the left of the drawings, whereas the porous material is positioned at the right of each figure. Fig. 3(a) indicates that porosity variation does not strongly influence the flow behavior, as also noted by Graminho and de Lemos [30] and de Lemos and Fischer [33]. On other hand, results for $\langle T_f \rangle^i$ (Fig. 3(b)) seems to indicate that an increase in porosity decreases the thermal boundary layer thickness at the wall, affecting the temperature distribution within the liquid phase with a substantial cooling effect located at the stagnation region. Also, as ϕ increases, a deeper cooling of the porous material is obtained (Fig. 3(c)), reflecting the fact that the cooling fluid penetrates more easily into the core of the layer as the void spaces become of a larger size.

Fig. 4 compares values for the Nusselt numbers calculated with the Local Thermal Equilibrium (LTE), Eq. (18), with those obtained

with the two-energy equation model (LTNE), Eq. (19). One can see in the figure that, for high porosities, no substantial difference is calculated when using the two models. However, for low void spaces or low porosity, the existence of more solid per total volume gives rises to distinct Nusselt numbers at the same axial location.

4.4. Effect of blockage ratio, h/H

A study of the influence of the porous layer thickness is now presented. Streamlines and temperature fields for various porous layer thicknesses, $Re = 750$ and $\phi = 0.90$ are presented in Fig. 5.

Fig. 5(a) shows that the porous layer thickness strongly influences the flow behavior, as also noted by [30,33]. The primary vortex has its strength diminished as h/H increases. Further, Fig. 5(b) shows that as the porous layer size increases, fluid temperature gradients at wall are reduced as more heat is transferred to the thicker solid phase. Fig. 5(c) also indicates that as h/H increases, temperature gradients of the solid and fluid phases tend towards the same value at the wall.

Fig. 6(a) compares Nusselt number calculated with the local thermal equilibrium model, Eq. (18), with those obtained with the local thermal non-equilibrium model, Eq. (19). It is observed that for porous layer thickness occupying 25% of the channel, a second peak on the local distribution of the Nusselt number is calculated with both models. For a porous layer thickness occupying 75% of the channel, such peak is smoothed out when applying both models. Differences in Nu for low h/H values occur due to the fact that, under such circumstances, temperature gradients are substantially different in both phases, as presented in Fig. 6(b), which was plotted for the second peak location at $x/B = 8$. Fig. 6(b) indicates that the greater the porous layer thickness, the more complete is the heat exchange between phases and, in turn, more realistic is the consideration of the Local Thermal Equilibrium hypothesis.

4.5. Effect of darcy number, Da

The effect of Darcy number, $Da = K/H^2$, is presented in Fig. 7. Streamlines displayed in Fig. 7(a) indicates that as Da decreases, fluid is pushed to flow above the porous layer in the gap of size $H - h$. Also noted is the reduction and elongation of the recirculation bubble, with fluid no longer penetrating the porous substrate as the permeability is reduced. Corresponding fluid and solid temperature distributions are plotted in Fig. 7(b) and (c), respectively. For high Da cases, the penetrating flow is sufficiently strong to deform temperature profiles leading to the formation of a thin boundary layer at the jet impinging region. As Da is reduced, the thermal boundary layer becomes thicker at the jet axis location and heat is transported through the porous material nearly by conduction. For $Da = 4.50 \times 10^{-5}$, the porous substrate behaves like a solid layer and a boundary layer forms at the macroscopic interface between the two media. Fig. 8 compares now values for the Nusselt numbers calculated with the Local Thermal Equilibrium (LTE) model with those obtained with the Local Thermal Non-Equilibrium (LTNE) hypothesis. It is observed that for high Da cases, as example for $Da = 6.75 \times 10^{-1}$, different Nusselt numbers are calculated depending on the energy model applied, with the 2EEM giving higher values along all channel. For low Da values, Nu is reduced for both models and tend towards the same value. When looking back at Fig. 7, one can see that temperature gradients at wall tend to equalize as Da decreases, leading to similar values for both Nu and Nu_f. In such cases, the mechanism of conduction heat transfer prevails in both the solid and fluid phases.

$$k_s/k_f = 10 \qquad k_s/k_f = 100 \qquad k_s/k_f = 200 \qquad k_s/k_f = 500$$
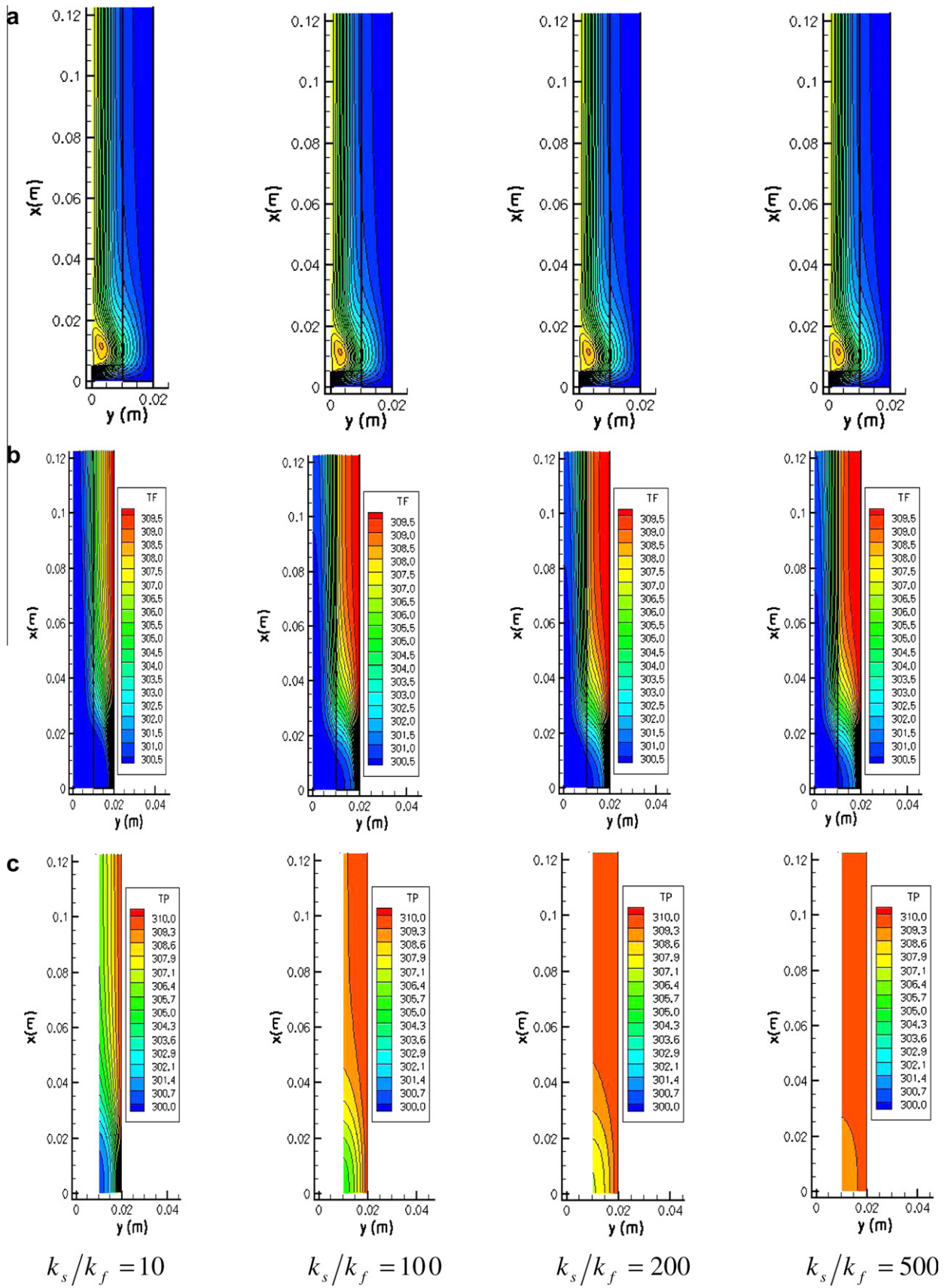
Fig. 9. Effect of k_s/k_f on temperature distributions for $Re = 750$, $H/B = 2$, $h = 0.5H$, $Da = 8.28 \times 10^{-3}$ and $\phi = 0.9$: (a) streamlines, (b) fluid temperature, (c) solid temperature.

4.6. Effect of thermal conductivity ratio, k_s/k_f

The effect of the ratio k_s/k_f is shown next. Fig. 9(a) indicates that k_s/k_f variation does not influence the flow behavior at all, since a decoupled solution is here applied, or say, the thermal field is solved with constant properties and no buoyancy effects are considered. Corresponding fluid and solid temperature distributions are plotted in Fig. 9(b) and (c), respectively. For high k_s/k_f cases, temperature gradients for both fluid and solid phases decreases since a higher solid thermal conductivity transport heat more easily through the solid, which, in turn, heats up the fluid via interfacial heat transfer. Fig. 10 shows the effect of k_s/k_f and energy model on the local distribution of Nusselt number. It is observed that for low k_s/k_f ratios, similar results with one and two-energy equation model are obtained since for low k_s/k_f values temperature profiles of fluid and solid phases are of same order. As such, consideration of Local Thermal Equilibrium hypothesis becomes more realistic. For high k_s/k_f values, the temperature filed become less equal (see Fig. 9) as heat is conducted quicker through the solid material, affecting, therefore, both temperature gradients at the wall, particularly at the stagnation point, $x \sim 0$.

4.7. Integral wall heat flux

As pointed out in de Lemos and Fischer [33], a useful parameter to assess the effectiveness in using a porous layer in the channel of Fig. 1(a) is to calculate the total heat transferred from the bottom wall. Such overall heat transferred from the lower wall can be calculated for both configurations presented in Fig. 1, as

$$q_w = \frac{1}{L} \int_o^L q_{wx}(x)dx \qquad (26)$$

Depending on the thermal model used, there are two possibilities to evaluate the local wall heat flux q_{wx}. One can use the hypothesis of Local Thermal Equilibrium (LTE), or else, individual terms can be applied in each phase in order to calculate the integrated heat transferred from the bottom wall. In the latter case, the LTNE model is employed.

Therefore, for the one-energy equation model, one has:

$$q_w = \frac{1}{L} \int_o^L q_{wx}(x)dx; q_{wx} = -k_{eff} \frac{\partial \langle T \rangle^i}{\partial y}\bigg|_{y=H}; \quad k_{eff} = \phi k_f + (1-\phi)k_s$$
$$(27)$$

and for the two-energy equation model:

$$q_w = \frac{1}{L} \int_o^L q_{wx}(x)dx; \quad q_{wx} = -\left[k_{eff,f} \frac{\partial \langle T_f \rangle^i}{\partial y}\bigg|_{y=H} + k_{eff,s} \frac{\partial \langle T_s \rangle^i}{\partial y}\bigg|_{y=H}\right];$$
$$\begin{cases} k_{eff,f} = \phi k_f \\ k_{eff,s} = (1-\phi)k_s \end{cases} \qquad (28)$$

For the cases where the a porous layer is considered, the wall hat flux is given a superscript ϕ on the form q_w^ϕ. The ratio q_w^ϕ/q_w can then be seen as a measure of the effectiveness in using a porous layer for enhancing or damping the amount of heat transferred through the wall.

Fig. 11 compares the ratio q_w^ϕ/q_w for several Reynolds number, porosities ϕ and blockage ratios h/H, with $k_s/k_f = 10$. Fig. 11 shows that for nearly all cases the one-energy equation model overesti-
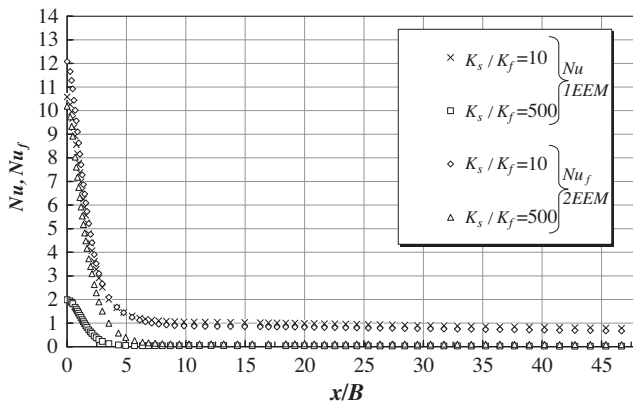

Fig. 10. Local Nusselt distribution as a function of energy model for various relation of k_s/k_f with $Re = 750$, $H/B = 2$, $k_s/k_f = 10$, $h = 0.5H$, $Da = 8.28 \times 10^{-3}$, $\phi = 0.9$.
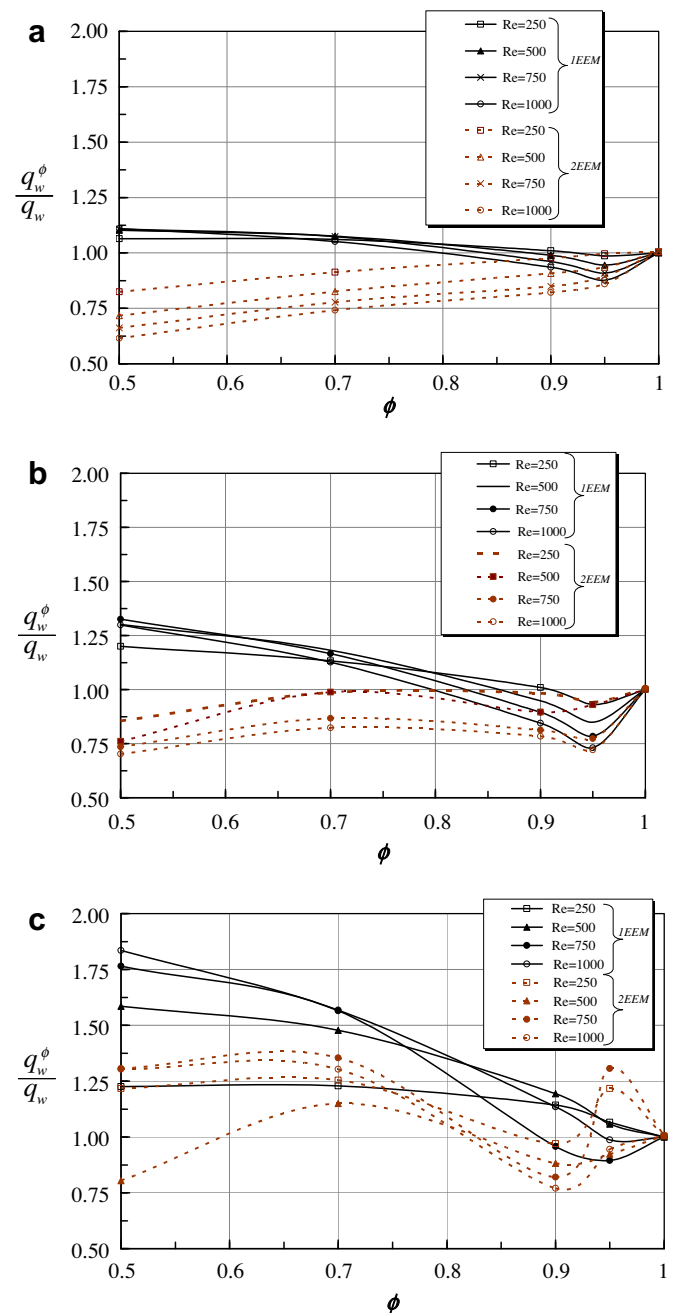

Fig. 11. Integral heat flux at the lower wall for various Reynolds and porosities with $H/B = 2$, $Da = 8.28 \times 10^{-3}$, and $k_s/k_f = 10$: (a) $h/H = 0.25$, (b) $h/H = 0.50$, (c) $h/H = 0.75$.
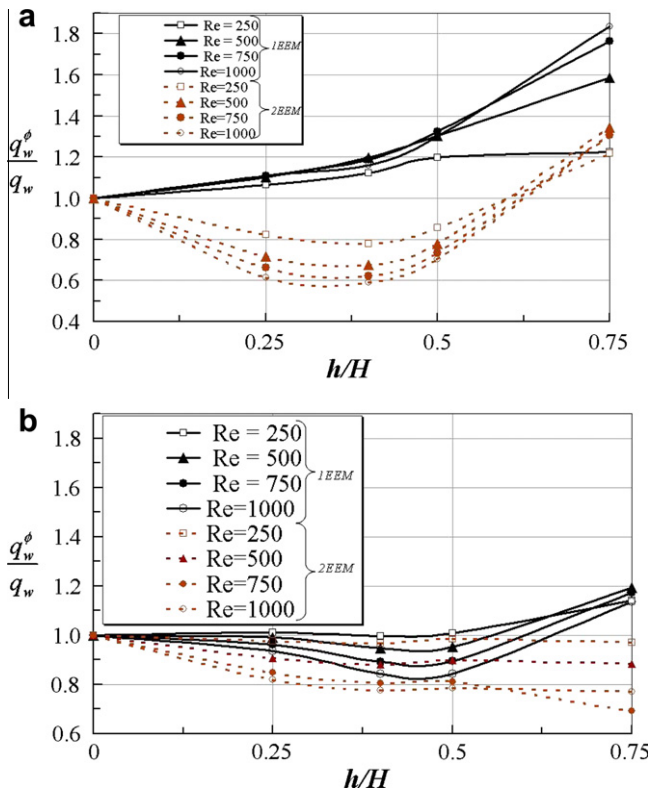
Fig. 12. Integral heat flux ratio at the lower wall for various Reynolds and porous layer thickness with $H/B = 2$, $Da = 8.28 \times 10^{-3}$, $k_s/k_f = 10$: (a) $\phi = 0.5$, (b) $\phi = 0.9$.
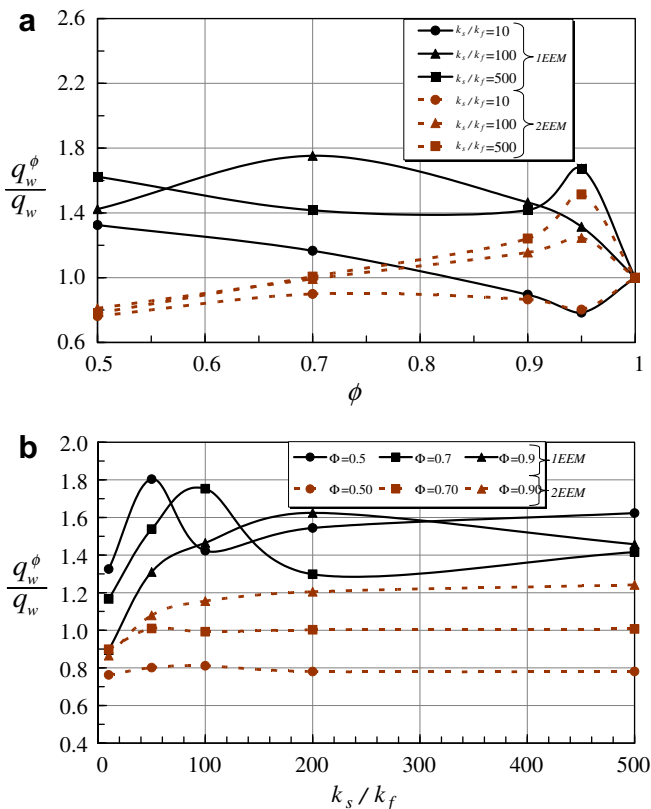

Fig. 13. Integral heat flux at the lower wall for various ratios k_s/k_f for $Re = 750$, $H/B = 2$ and $Da = 8.28 \times 10^{-3}$.

mates the integral heat transferred from the bottom wall, except for $\phi > 0.9$. For such high porosity cases, both one and two-energy equation models give similar results since contribution of the solid phase to the overall wall heat transport is small, leading to more realistic results when using the LTE model.

Fig. 12 further shows variations for the integral wall heat flux ratio with h/H for two values of porosity ϕ. For a porous medium with low porosities or more solid material (Fig. 12(a)), results indicate a substantially different ratio q_w^ϕ/q_w for the two models, being advantageous to use ticker layers only, or say, $q_w^\phi/q_w > 1$ only when $h/H > 0.63$. For high porosities (Fig. 12(b)), results indicate a reasonably good agreement between the two models for up to $h/H = 0.5$. Fig. 12(b) further indicates that the use of a porous layer brings no advantages, a result obtained when using the LNTE model and the parameters here considered.

Fig. 13 finally compiles results for q_w^ϕ/q_w when the thermal conductivity ratio k_s/k_f and porosity ϕ are varied. It is observed that the one-energy equation model overestimates the wall heat flux in the majority of the cases. Fig. 13(a) shows that for porosities varying from $\phi = 0.9$ to $\phi = 1.0$ results indicate a good agreement between the two models compared. Also shown is that for $\phi = 0.9$ the presence of a porous layer is beneficial for k_s/k_f greater than 10, since the ratio q_w^ϕ/q_w for such condition is greater than 1. However, one should emphasize that differences between the two models are here obtained under the assumptions mentioned earlier, or say, neglect of tortuosity and local conduction when the LTE and LNTE hypotheses are applied, respectively. These mechanisms might play a certain role on the accuracy of the predictions with the two models.

5. Conclusions

This paper investigated the structure of fluid and thermal fields for an impinging laminar jet into a porous bed. Effects of variation of porosity, permeability, channel blockage ratio and solid-to-fluid thermal conductivity ratio were investigated. The following conclusions were observed

(1) The presence of a porous bed on the plate eliminates the second peak in distribution of local Nusselt number and allows for controlling heat transfer from the wall, a feature also confirmed by de Lemos and Fischer [33].

(2) Porosity does not strongly influence flow behavior, but affects temperature fields by better cooling the solid matrix as ϕ increases, particularly at the stagnation region. For low porosity materials, the fluid Nusselt number differ when calculations use LTE or LNTE model, with Nu approaching Nu_f when increasing porosity.

(3) For thinner porous layers, the flow field approaches that of an empty channel with a large recirculating bubble attached to the jet entrance. Temperatures fields for fluid and solid become identical for a large h/H value as there is more room for thermal equilibrium to be established.

(4) For highly permeable media, the fluid penetrates the porous substrate and a rerirculation bubble remains attached to the nozzle while thermal boundary layer thickness is reduced with corresponding reduction of the solid cooling effect. Less permeable porous media tend to make both temperature gradients at the wall to attain similar values as small convective currents do not cause substantial temperature difference close to the wall.

(5) For high k_s/k_f ratios, temperature levels remain high at the solid phase, increasing, consequently, fluid temperatures and, in addition, thickening the thermal boundary layer at the wall.

(6) For low porosities, thicker porous layers and low thermal conductivity ratios, discrepancies when using both energy models appear when calculating q_w^ϕ/q_w. Such discrepancies, however, might be dependent on the assumptions of neglecting the mechanisms of tortuosity and local conduction.

(7) The use of the LNTE model indicates that it is advantageous to use a layer of highly conducting and highly porous material attached to the cooled wall. However, these conclusions are based under the assumption of neglecting the mechanisms of tortuosity and dispersion within the porous material.

Acknowledgements

References

[1] R. Gardon, J.C. Akfirat, Heat transfer characteristics of impinging two-dimensional air jets, J. Heat Transfer 101 (1966) 101–108.

[2] E.M. Sparrow, T.C. Wong, Impinging transfer coefficients due to initially laminar slot jets, Int. J. Heat Mass Transfer 18 (1975) 597–605.

[3] M. Chen, R. Chalupa, A.C. West, V. Modi, High Schmidt mass transfer in a laminar impinging slot jet, Int. J. Heat Mass Transfer 43 (2000) 3907–3915.

[4] V.A. Chiriac, A. Ortega, A numerical study of the unsteady flow and heat transfer in a transitional confined slot jet impinging on an isothermal surface, Int. J. Heat Mass Transfer 45 (2002) 1237–1248.

[5] Y. Zhang, X.F. Peng, I. Conte, Heat and mass transfer with condensation in non-saturated porous media, Numer. Heat Transfer Part A – Appl. 52 (2007) 1081–1100.

[6] M.E. Taskin, A.G. Dixon, E.H. Stitt, CFD study of fluid flow and heat transfer in a fixed bed of cylinders, Numer. Heat Transfer Part A – Appl. 52 (3) (2007) 203–218.

[7] T. Basak, S. Roy, H.S. Takhar, Effects of nonuniformly heated wall(s) on a natural-convection flow in a square cavity filled with a porous medium, Numer. Heat Transfer Part A – Appl. 51 (10) (2007) 959–978.

[8] J. Eriksson, S. Ormarsson, H. Petersson, Finite-element analysis of coupled nonlinear heat and moisture transfer in wood, Numer. Heat Transfer Part A – Appl. 50 (9) (2006) 851–864.

[9] V. Bubnovich, L. Henriquez, N. Gnesdilov, Numerical study of the effect of the diameter of alumina balls on flame stabilization in a porous-medium burner, Numer. Heat Transfer Part A – Appl. 52 (3) (2007) 275–295.

[10] X.B. Chen, P. Yu, S.H. Winoto, H.T. Low, Free convection in a porous wavy cavity based on the Darcy–Brinkman–Forchheimer extended model, Numer. Heat Transfer Part A – Appl. 52 (4) (2007) 377–397.

[11] N. Yucel, R.T. Guven, Forced-convection cooling enhancement of heated elements in a parallel-plate channels using porous inserts, Numer. Heat Transfer Part A – Appl. 51 (3) (2007) 293–312.

[12] L. Betchen, A.G. Straatman, B.E. Thompson, A non-equilibrium finite-volume model for conjugate fluid/porous/solid domains, Numer. Heat Transfer Part A – Appl. 49 (6) (2006) 543–565.

[13] Y.W. Zhang, Non-equilibrium modeling of heat transfer in a gas-saturated powder layer subject to a short-pulsed heat source, Numer. Heat Transfer Part A – Appl. 50 (6) (2006) 509–524.

[14] C.R. Ruivo, J.J. Costa, A.R. Figueiredo, Analysis of simplifying assumptions for the numerical modeling of the heat and mass transfer in a porous desiccant medium, Numer. Heat Transfer Part A – Appl. 49 (9) (2006) 851–872.

[15] F. Moukalled, Y. Saleh, Heat and mass transfer in moist soil, part I. Formulation and testing, Numer. Heat Transfer Part A – Appl. 49 (5) (2006) 467–486.

[16] X.H. Wang, M. Quintard, G. Darche, Adaptive mesh refinement for one-dimensional three-phase flow with phase change in porous media, Numer. Heat Transfer Part B – Fund. 50 (3) (2006) 231–268.

[17] X.H. Wang, M. Quintard, G. Darche, Adaptive mesh refinement for one-dimensional three-phase flow with phase change in porous media, Numer. Heat Transfer Part A – Appl. 50 (4) (2006) 315–352.

[18] A. Mansour, A. Amahmid, M. Hasnaoui, M. Bourich, Multiplicity of solutions induced by thermosolutal convection in a square porous cavity heated from below and submitted to horizontal concentration gradient in the presence of Soret effect, Numer. Heat Transfer Part A – Appl. 49 (1) (2006) 69–94.

[19] A.V. Kuznetsov, L. Cheng, M. Xiong, Effects of thermal dispersion and turbulence in forced convection in a composite parallel-plate channel: Investigation of constant wall heat flux and constant wall temperature cases, Numer. Heat Transfer Part A – Appl. 42 (4) (2002) 365–383.

[20] B.M.D. Miranda, N.K. Anand, Convective heat transfer in a channel with porous baffles, Numer. Heat Transfer Part A – Appl. 46 (5) (2004) 425–452.

[21] N.B. Santos, M.J.S. de Lemos, Flow and heat transfer in a parallel-plate channel with porous and solid baffles, Nume. Heat Transfer Part A – Appl. 49 (5) (2006) 471–494.

[22] M. Assato, M.H.J. Pedras, M.J.S. de Lemos, Numerical solution of turbulent channel flow past a backward-facing-step with a porous insert using linear and non-linear k-ε models, J. Porous Media 8 (1) (2005) 13–29.

[23] S.Y. Kim, A.V. Kuznetsov, Optimization of pin-fin heat sinks using anisotropic local thermal non-equilibrium porous model in a jet impinging channel, Numer. Heat Transfer Part A – Appl. 44 (8) (2003) 771–787.

[24] P. Xiang, A.V. Kunetsov, A.M. Seyam, A porous medium model of the hydroentanglement process, Int. J. Heat Mass Transfer 11 (2008) 35–49.

[25] P. Xiang, A.V. Kunetsov, Simulation of shape dynamics of a long flexible fiber in a turbulent flow in the hydroentanglement process, Int. J. Heat Mass Transfer 35 (2008) 529–534.

[26] M. Prakash, F.O. Turan, Y. Li, J. Manhoney, G.R. Thorpe, Impinging round jet studies in a cilindrical enclosure with and without a porous layer: Part I: Flow visualizations and simulations, Chem. Eng. Sci. 56 (2001) 3855–3878.

[27] M. Prakash, F.O. Turan, Y. Li, J. Manhoney, G.R. Thorpe, Impinging round jet studies in a cilindrical enclosure with and without a porous layer: Part II: DLV measurements and simulations, Chem. Eng. Sci. 56 (2001) 3879–3892.

[28] W.-S. Fu, H.-C. Huang, Thermal performance of different shape porous blocks under an impinging jet, Int. J. Heat Mass Transfer 40 (10) (1997) 2261–2272.

[29] T.-Z. Jeng, S.-C. Tzeng, Numerical study of confined slot jet impinging on porous metallic foam heat sink, Int. J. Heat Transfer 48 (2005) 4685–4694.

[30] D.R. Graminho, M.J.S. de Lemos, Laminar confined impinging jet into a porous layer, Numer. Heat Transfer, Part A: Appl. 54 (2) (2008) 151–177.

[31] M.J.S. de Lemos, Turbulence in Porous Media: Modeling and Applications, Elsevier, Kidlington, 2006.

[32] F.D. Rocamora Jr., M.J.S. de Lemos, Analysis of convective heat transfer of turbulent flow in saturated porous media, Int. Commun. Heat Mass Transfer 27 (6) (2000) 825–834.

[33] M.J.S. de Lemos, C. Fischer, Thermal analysis of an impinging jet on a plate with and without a porous layer, Numer. Heat Transfer Part A 54 (2008) 1022–1041.

[34] W.G. Gray, P.C.Y. Lee, On the theorems for local volume averaging of multiphase system, Int. J. Multiphase Flow 12 (1977) 401–410.

[35] M.B. Saito, M.J.S. de Lemos, Interfacial heat transfer coefficient for non-equilibrium convective transport in porous media, Int. Commun. Heat Mass Transfer 32 (5) (2005) 666–676.

[36] N. Wakao, S. Kaguei, T. Funazkri, Effect of fluid dispersion coefficients on particle-fluid heat transfer coefficient in packed bed, Chem. Eng. Sci. 34 (1979) 325–336.

[37] F. Kuwahara, M. Shirota, A. Nakayama, A numerical study of interfacial convective heat transfer coefficient in two-energy equation model for convection in porous media, Int. J. Heat Mass Trasfer 44 (2001) 1153–1159.

[38] M.B. Saito, M.J.S. de Lemos, A correlation for interfacial heat transfer coefficient for turbulent flow over an array of square rods, J. Heat Transfer 128 (2006) 444–452.

[39] B. Alazmi, K. Vafai, Analisys of variants within the porous media transport models, J. Heat Transfer 122 (2000) 303–326.

[40] S.V. Patankar, Numerical Heat Transfer and Fluid Flow, Hemisphere, New York, 1980.